

Charge carrier dynamics and photocatalytic activity of {111} and {100} faceted Ag_3PO_4 particles

Rochan Sinha¹, Dennis Friedrich², Georgios Zafeiropoulos¹, Erwin Zoethout¹, Matteo Parente¹, Mauritius C. M. van de Sanden^{1,3}, Anja Bieberle-Hütter^{1,}*

¹Dutch Institute for Fundamental Energy Research (DIFFER), P.O. Box 6336, 5600 HH Eindhoven, the Netherlands

²Institute for Solar Fuels, Helmholtz-Zentrum Berlin für Materialien und Energie GmbH, Hahn-Meitner-Platz 1, 14109 Berlin, Germany

³Department of Applied Physics, Eindhoven University of Technology (TU/e), P.O. Box 513, 5600 MB Eindhoven, the Netherlands

*Corresponding author. Email: a.bieberle@diffier.nl

ABSTRACT

Silver orthophosphate (Ag_3PO_4) is a highly promising visible light photocatalyst with high quantum yield for solar driven water oxidation. Recently, the performance of this material has been further enhanced using facet-controlled synthesis. The tetrahedral particles with {111} exposed facets demonstrate higher photocatalytic performance than the cubic particles with {100} exposed facets. However, the reason behind this large difference in photocatalytic performance is still not understood. In this work, we study the free charge carrier dynamics, such as mobility, lifetime, and diffusion lengths, for the {111}-faceted tetrahedral and the {100}-faceted cubic particles using time-resolved microwave conductivity (TRMC) measurements. An order of magnitude higher charge carrier mobility and diffusion length is found for the tetrahedral particles as compared to the cubic particles. The differences in crystal structure, surface composition, and optical properties are investigated in order to understand how these properties impact the charge carrier dynamics and the photocatalytic performance of the differently faceted particles.

INTRODUCTION

The advent of climate change and the ever-increasing CO₂ concentration in the atmosphere has made the search for a carbon-neutral source of chemical fuels a 'holy grail' in terms of renewable energy research. One attractive route to obtain hydrogen, which is an important fuel and chemical feedstock, is by direct splitting of water with solar energy using an efficient photocatalytic material. The fuels obtained in this way are known as 'solar fuels'¹. However, the solar-to-hydrogen efficiency is very low for photocatalytic materials. The main reason for the limited efficiency is the four-electron oxygen evolution reaction (OER) which is kinetically challenging compared to the two-electron hydrogen evolution reaction (HER). Thus, development of efficient, stable, inexpensive, and abundant photocatalytic materials which show high OER production is a significant bottleneck for developing viable water splitting systems²⁻⁴.

One promising material which has emerged as a highly performing photocatalyst for water splitting is silver orthophosphate (Ag₃PO₄). It was first studied by Yi et al.⁵ who demonstrated that Ag₃PO₄ has a bandgap of approximately 2.4 eV and a very high quantum yield (> 90%) for wavelengths lower than 480 nm. The oxygen evolution rates were higher than those of other visible light photocatalysts, such as BiVO₄ and WO₃⁶. One possible reason for the high performance was proposed to be the large difference in the effective electron mass and hole mass for bulk Ag₃PO₄⁷. This leads to significantly different mobility for the electrons and holes which results in a lower recombination rate and is one rationale for the good photocatalytic performance of Ag₃PO₄.

Another possible reason for the high oxygen evolution rate is that Ag₃PO₄ possesses a very deep valence band, located approximately +2.9 V vs. NHE (Normal Hydrogen Electrode, pH 0). Therefore, it has a large photovoltage for efficient splitting of water to O₂⁵. However, the conduction band is located at +0.45 V vs. NHE (pH 0) which means that it cannot reduce water to H₂⁸. Therefore, in order to perform the OER process this material requires the use of a sacrificial reagent, such as silver nitrate (AgNO₃) which has a redox level below the conduction band of Ag₃PO₄.

The intrinsic good water oxidation performance was further improved by facet engineering of Ag₃PO₄ particles. Martin et al.⁹ and Bi et al.¹⁰ demonstrated shape-controlled synthesis of Ag₃PO₄ particles with controlled exposure of certain facets, such as tetrahedral particles with {111} facets and cubic particles with {100} facets. The tetrahedral particles showed the highest OER rate among all photocatalytic materials active in visible light⁶ and an order of magnitude better performance than cubic particles.

Theoretical studies attributed the high performance of the {111}-faceted tetrahedral Ag₃PO₄ particles to reasons, such as a higher surface energy at this surface⁹, a lower free energy required for dehydrogenation of water⁹, or a lower charge redistribution during OER at the {111} surface as compared to the {100} and {110} surfaces¹¹. It was also proposed that the exposed phosphorus atoms on the Ag₃PO₄ {111} surface promote the dehydrogenation of H₂O and reduce the formation of mid-bandgap states.⁷ Furthermore, different surface compositions of the {111}- and the {100}-faceted particles can lead to different band bending and, in consequence, to different performance^{12,13}. Another theoretical work by Umezawa et al.¹⁴ explored the difference in the effective masses for the {111} and {100} facets of Ag₃PO₄ as a possible reason for the better charge carrier properties and therefore photocatalytic performance of the tetrahedral particles compared to the cubic particles. The difference in charge carrier transport properties of the differently faceted Ag₃PO₄ particles could contribute to the differences in their photocatalytic performance.

In contrast to the various theoretical studies on this topic, only one experimental work has previously attempted to explore the effect of different facets on the charge carrier dynamics and

photocatalytic properties¹⁵. In that study, lower photocatalytic activity and charge carrier lifetime was found for the tetrahedral as compared to the cubic Ag₃PO₄. It is not clear why lower performance for the tetrahedral particles was observed when compared to previous studies^{9,16}.

Hence, in order to elucidate the effect of charge carrier dynamics of differently faceted Ag₃PO₄ particles, we fabricate {111}-faceted tetrahedral and {100}-faceted cubic Ag₃PO₄ particles in this study and analyze the charge carrier dynamics using time-resolved microwave conductivity (TRMC) measurements. We find that tetrahedral particles demonstrate superior charge carrier dynamics and we relate this to the morphology, structure, chemical composition, and optical properties of the particles. The better charge carrier dynamics leads to the higher photocatalytic performance of the tetrahedral particles compared to the cubic particles.

EXPERIMENTAL METHODS

Synthesis of tetrahedral and cubic Ag₃PO₄ particles

The synthesis of the tetrahedral and cubic particles was performed by a modified version of the process used by Martin et al.⁹ and Bi et al.¹⁰ Utmost care was taken to insure that the synthesised particles were not exposed to any light source, either during or after the process.

For tetrahedral particles, 12 mmol of AgNO₃ (99% purity) was dissolved in 80 ml of ethanol (95% purity, Merck Schuchardt) under rapid stirring (1000 rpm). Simultaneously, 20 ml of H₃PO₄ (85% purity, Acros Organics) was mixed thoroughly with 80 ml ethanol under similarly vigorous stirring. After both products were separately dissolved and both solutions became transparent, the AgNO₃-ethanol mixture was added drop-wise to the H₃PO₄-ethanol solution. An instantaneous precipitate formed under stirring and then rapidly disappeared. Addition of AgNO₃-ethanol was continued until the H₃PO₄-ethanol solution turned slightly cloudy (usually around 10 ml of the former is required for the precipitation). A few drops of this H₃PO₄-ethanol + AgNO₃-ethanol suspension was added back into the AgNO₃-ethanol solution. The previously clear AgNO₃-ethanol solution yielded then an instantaneously bright yellow Ag₃PO₄ precipitate. After 1 h of stirring, the solution turned into a bright green colour indicating the growth and shape change of the Ag₃PO₄ particles. After washing with ethanol and centrifuging for three times, the photocatalyst was placed in a desiccator for 48-72 h to ensure that all moisture was removed from the catalyst.

For the synthesis of the cubic particles, 0.45 g (0.053M) AgNO₃ was dissolved in 50 ml deionized (DI) water. Meanwhile in a separate vial, 0.069 cm³ NH₃·H₂O was added dropwise to 10 ml DI water. The ammonia solution was then added to the silver nitrate solution to which the resulting solution turned first brown (Ag₂O) and then transparent [Ag(NH₃)₂]⁺. To this transparent solution, 0.15 M of aqueous Na₂HPO₄ solution was added until the solution appeared yellow-green. The solution was stirred for 2 h at 1000 rpm using a magnetic stirrer-bar/plate and was subsequently washed and centrifuged 3 times to remove any unreacted product. Drying was done either in a desiccator for 48-72 h or in a drying oven at 70°C for 20 min. No differences in the properties were seen with the different drying methods.

Photocatalytic measurement

A Hiden QGA quadrupole mass spectrometer (MS) operating in selected ion mode with a SEM detector was used for the detection of oxygen. For a typical oxygen evolution experiment, 0.1 g of Ag₃PO₄ powder was dispersed in 150 ml of DI water with an additional amount of 0.45 g AgNO₃ acting as an electron acceptor. The whole reaction was carried out in a 3-necked glass flask which was sealed with septum covers. Before the solution was irradiated, the reactor was thoroughly

purged with He (99.999% purity, 32 sccm) to remove all oxygen in the headspace of the reactor and dissolved oxygen in water. A baseline was taken for 2-3 h to ensure a minimum amount of oxygen in the system. Illumination was provided by an AM 1.5 class A solar simulator (LCS 100, Oriel Instruments) using a 100 W Xe lamp with a calibrated illumination intensity of 100 mW cm⁻² at the sample position (Reference cell 91150V, Newport). The light was turned on and the partial pressure of O₂ (molecular weight = 32) was measured for at least 1 h. Then, the light was switched off and helium was flowed until the partial pressure of O₂ (pO₂) reached to baseline levels again. The measured pO₂ was compared to a standard 1% O₂ in He mixture which was flown at the same rate (32 sccm). This mixture has a known O₂ concentration of 10,000 ppm. Using the flow rate and the pO₂ of the standard O₂ mixture and knowing the weight of the Ag₃PO₄ powder, the amount of oxygen evolved in the system was determined in terms of μmol h⁻¹ g⁻¹.

Physico-chemical characterization

The morphologies of the Ag₃PO₄ particles on Si substrate were examined by field emission scanning electron microscope (SEM) (Zeiss Sigma) with an in-lens detector and 5 kV accelerating voltage. Structural characterization was done on dried Ag₃PO₄ particles in powdered form. It was performed using a Bruker D8 Eco X-ray diffractometer (XRD) with a Cu Kα (λ= 1.5406 Å) source and a Lynx-eye detector in a Bragg-Brentano (θ - 2θ) configuration in the 2θ range from 20° to 72°. A Thermo Scientific K-Alpha X-ray photoelectron spectroscopy (XPS) setup equipped with a monochromatic Al Kα source (hν = 1486.6 eV) was used for the chemical analysis. The Ag₃PO₄ particles were drop-casted on FTO substrate for the measurement. The binding energy was corrected with respect to the adventitious carbon C 1s peak at 284.8 eV. The optical absorbance of the Ag₃PO₄ on a glass substrate was characterized with a Perkin Elmer 1050 UV/Vis/NIR spectrophotometer in the wavelength range of 300 nm to 900 nm.

Time-resolved microwave conductivity (TRMC) measurements

TRMC measurements were performed on Ag₃PO₄ particles on a quartz substrate by mounting the samples in a microwave cavity cell and placing the cell within a setup similar to the one described elsewhere.^{17,18} A voltage controlled oscillator (SiversIMA VO3262X) generated the microwaves (X-band region, 8.4–8.7 GHz). During the measurements, a change in the microwave power ($\Delta P/P$) reflected by the cavity upon sample excitation by 3 ns (full-width at half-maximum) pulses of a Q-switched Nd: YAG laser at a wavelength of 410 nm (10 Hz repetition rate) was monitored and correlated to the photoinduced change in the conductance of the sample, ΔG . The relation between the change in microwave power and the photoconductance and relation of photoconductance to the sum of electron and hole mobilities ($\Sigma\mu$) is given by Eq. S1 and S2, respectively, in the supporting information.

RESULTS

Particle morphology

Tetrahedral-shaped Ag₃PO₄ particles with {111} exposed facets and cubic-shaped Ag₃PO₄ particles with {100} exposed facet were synthesised using a modified version of the procedure developed by Martin et al.⁹ (refer to experimental methods). The synthesis results in a high-purity yield with only tetrahedral or cubic Ag₃PO₄ particles, respectively, as shown in Figures 1(a) and 1(b). Negligible amounts of irregular particles or particles with other shapes can be seen and are related to unreacted chemicals during the synthesis which were not completely removed during the purification process.

The particle size distribution was found to be $1449 \text{ nm} \pm 612 \text{ nm}$ for the cubic particles and $545 \text{ nm} \pm 242 \text{ nm}$ for the tetrahedral particles (Table 1). Thus, the cubic particles were almost three times larger in size than the tetrahedral particles. Both, the difference in size of the particles as well as the broad size distribution, are comparable to what was reported in the literature.^{9,19,20}

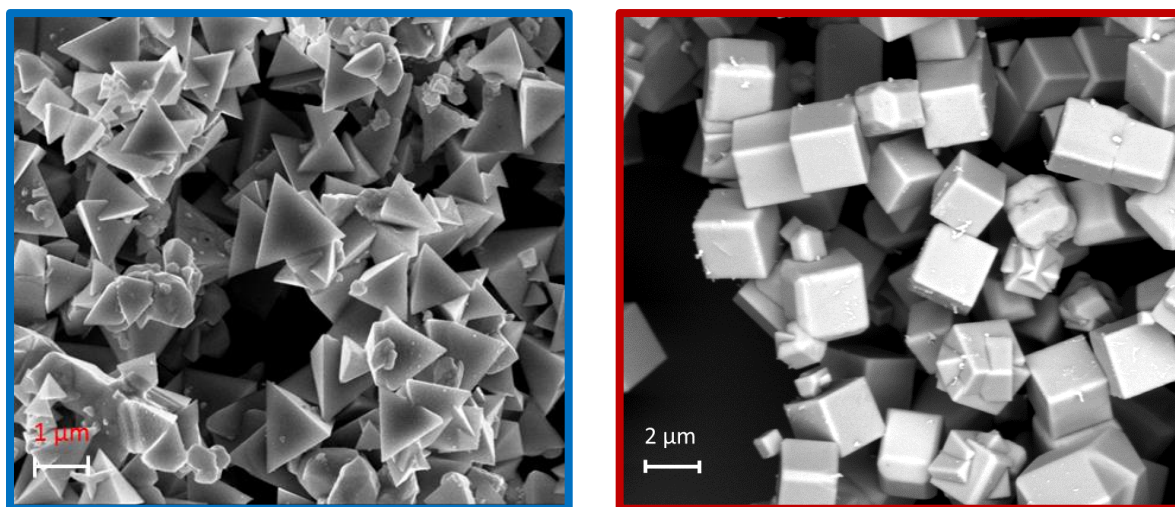


Figure 1 SEM micrographs of (a) tetrahedral and (b) cubic Ag_3PO_4 particles.

Crystalline structure

XRD diffractograms for both syntheses show polycrystalline Ag_3PO_4 (6.004 \AA , BCC, P_{-43n} , ICSD number: 14000) (Figure S1 in the supporting information). The variation in the crystallographic peak intensity ratios are used to confirm the differences in the type of exposed facet of the two morphologies. Namely, tetrahedral Ag_3PO_4 particles have an intensity ratio of 0.97 between $\{222\}$ and $\{200\}$ planes, whereas cubic structures have a ratio of 0.71. Following the theory proposed by Wang et al.,²¹ this confirms that the tetrahedral particles are comprised of $\{111\}$ facets. Furthermore, the peak intensity ratio between $\{110\}$ and $\{200\}$ for the cubic particles is 0.57, which confirms according to Martin et al. that the cubic structures are composed of $\{100\}$ facets.⁹ The crystallite size of the particles was calculated by Scherrer analysis for the highest intensity $\{210\}$ peak and was 106 nm for the cubic and 53 nm for the tetrahedral particles, respectively (Table 1).

Photocatalytic performance

The oxygen evolution rates of the cubic and the tetrahedral particles were measured using mass spectrometry in the presence of an electron scavenger under 1-sun illumination (Table 1). The tetrahedral particles have an oxygen evolution rate of $212 \mu\text{mol h}^{-1} \text{ g}^{-1}$ which is 1.6 times higher than the rate of $135 \mu\text{mol h}^{-1} \text{ g}^{-1}$ observed for the cubic particles. The oxygen evolution rates reported in this study are lower than the highest reported values in literature ($6074 \mu\text{mol h}^{-1} \text{ g}^{-1}$ and $605 \mu\text{mol h}^{-1} \text{ g}^{-1}$ for the tetrahedral and cubic particles, respectively, by Martin et al.⁶). The lower photocatalytic performance for the tetrahedral particles in this study as compared to that obtained by Martin et al. has also been observed in other studies with comparable or even lower photocatalytic performance when compared to the cubic particles.^{15,20} In our study, we relate the lower oxygen evolution rate mainly to the lower illumination intensity (100 mW cm^{-2} in this study versus 500 mW cm^{-2} in Martin et al.⁹). Previous work on the relation of photocatalytic reaction rate and light intensity shows a linear relationship at lower light intensities which then saturates at

higher intensities.^{22,23} Thus, we can speculate that the oxygen evolution rate could be up to 5 times higher than what we obtain here if a light source with higher intensity was used. We note that differences in the oxygen evolution rate can also be related to other factors, such as scattering of the light by the particles and the design of the reactor.

Table 1 Particle sizes (from SEM), crystallite sizes (from XRD), and oxygen evolution rates (from mass-spectrometry) for the tetrahedral and cubic Ag_3PO_4 particles, respectively.

Particle type	Particle size (nm)	Crystallite size (nm)	Oxygen evolution rate ($\mu\text{mol h}^{-1} \text{g}^{-1}$)
Tetrahedral	545 \pm 242	53	212
Cubic	1449 \pm 612	106	135

To understand the difference in photocatalytic activity of the tetrahedral and cubic particles, the differences in their optical properties, surface composition, and charge carrier dynamics are investigated in the following.

Optical properties

The optical properties were studied using UV-Vis diffuse reflectance spectroscopy as shown in Figure 2 (a). The diffuse reflectance for both materials drops rapidly below 530 nm which corresponds to the onset of absorption. Ag_3PO_4 is known to be an indirect bandgap semiconductor⁵. The band gap values for the tetrahedral and cubic particles were obtained from Kubelka-Munk plots²⁴ and were 2.45 eV for the tetrahedral and 2.43 eV for the cubic particles (Figures 2 (b) and (c), respectively). These bandgap values are rather close to each other which is related to the fact that the bulk material is the same for both tetrahedral particles and only the exposed facets are different. This similarity in bandgap for the two different particles has also been reported in the literature previously^{9,20,25,26}. Hence, it can be concluded that differences in photocatalytic properties are not merely related to the optical properties.

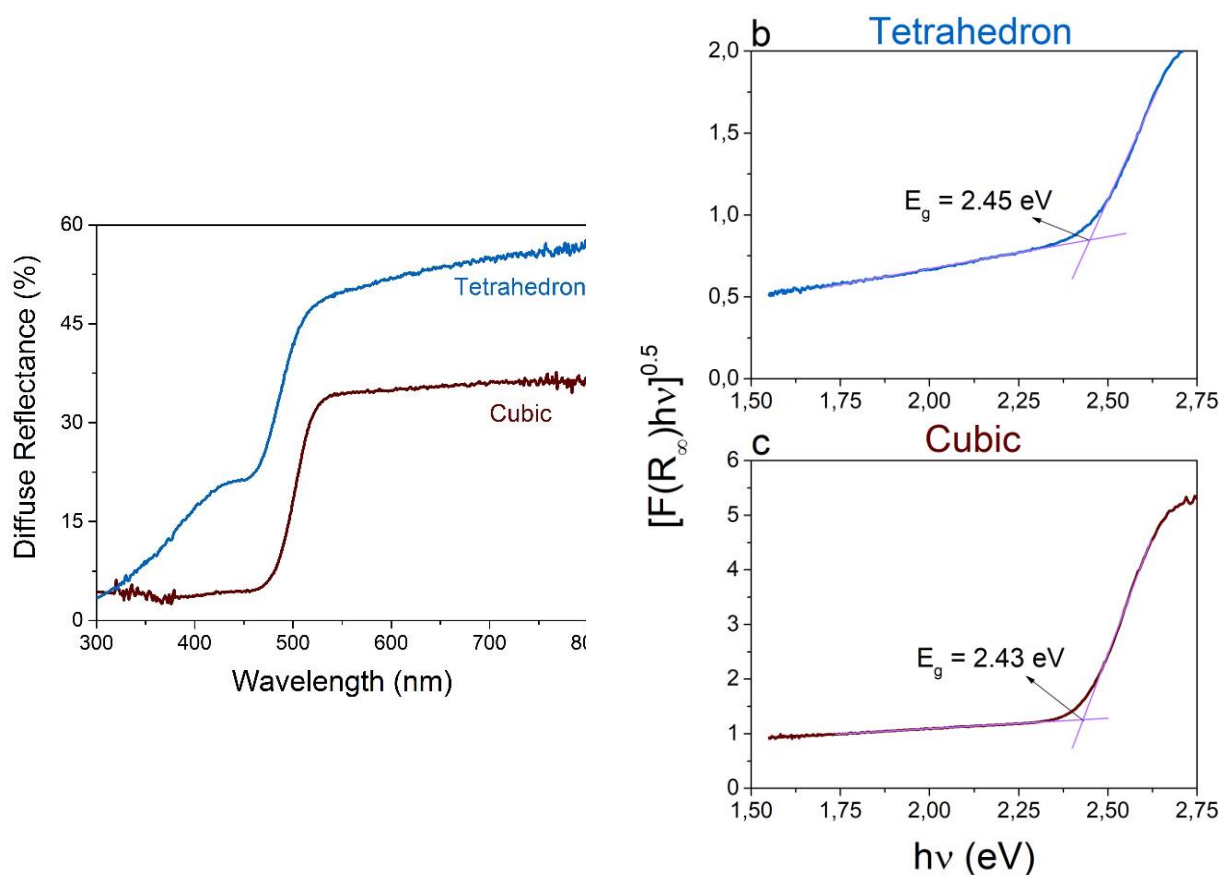


Figure 2 (a) UV-Vis diffuse reflectance spectra of the tetrahedral and cubic Ag_3PO_4 particles. The dotted line represents the onset of absorption; Kubelka-Munk plot, $[F(R_\infty)hv]^{0.5}$ versus energy ($h\nu$) for calculating the indirect bandgap for (b) tetrahedral and (c) cubic particles, respectively. The linear fitting curves used to obtain bandgap value (E_g) are shown as purple lines.

Surface composition

The effect of the difference in exposed facet on the surface composition of the Ag_3PO_4 tetrahedral and cubic particles was studied with X-ray photo-electron spectroscopy (XPS) as shown in Figure 3(a) and (b), respectively. The XPS survey spectra show the elements Ag, P, and O which are present in Ag_3PO_4 along with small amounts of C and Sn. The latter is observed as a result of the fluorine-doped tin oxide (F: SnO_2) substrate, on which the Ag_3PO_4 particles were drop-casted for performing the XPS analysis. The Ag $3d_{5/2}$ peak for both cubic and tetrahedral particles is found at a binding energy value of 267.9 eV according to the high-resolution Ag 3d spectra in Figure S2 in the supporting information. This peak position is attributed to the Ag(I) oxidation state and corresponds to Ag^+ ions in Ag_3PO_4 . Reduction to the Ag (0) metal state would result in a shift of the $3d_{5/2}$ peak to a higher binding energy of 368.6 eV, which is not observed here.

From the atomic concentrations of the different elements (insets in Figure 3(a) and (b)), the Ag : P ratio was found to be approximately 3.2 : 1 for the cubic particles and 2.1 : 1 for the tetrahedral particles. In the ideal case, the ratio should be 3 : 1. This suggests that the surface of the cubic particles is slightly Ag-rich while the surface of the tetrahedral particles is highly P-rich. This agrees well with Ma et al. ⁷ who reported Ag and O terminated {100} (cubic) surface and the presence of P and O at the outermost layer of the {111} (tetrahedral) surface.

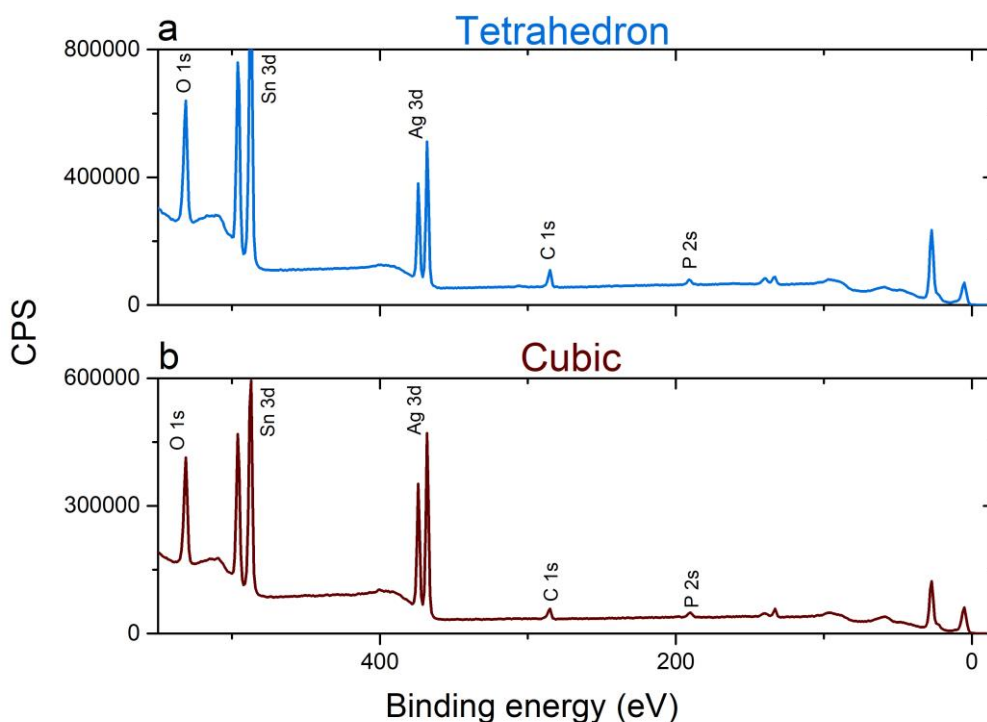


Figure 3 X-ray photo-electron survey spectra for (a) tetrahedral and (b) cubic Ag_3PO_4 particles. The atomic concentration (At. %) for the elements present on the particle surface is shown in tabular form.

Charge carrier dynamics

The effect of different exposed facets on the charge carrier dynamics of the Ag_3PO_4 particles was studied by time-resolved microwave conductivity (TRMC).¹⁷ Ag_3PO_4 particles coated onto a quartz substrate were excited with a nano-second laser pulse and the resulting light-induced change in the reflected microwave power was monitored. The TRMC signal thus obtained is represented as the product of the absorbance-normalised quantum yield (ϕ) and the sum of the mobilities of free charge carriers in the Ag_3PO_4 ($\sum\mu_i$) for different intensities (see experimental section for details). Assuming that the internal quantum yield (ϕ) is close to unity and that no recombination occurs within the response time of the setup (9 ns), the peak value of the TRMC signal ($(\phi\sum\mu_i)_{\text{peak}}$) yields the total mobility (μ_{total}), which is the sum of the charge carrier mobilities of the electrons and holes. The fitting of the TRMC signal decay provides the charge carrier lifetime (τ). It should be noted that the μ_{total} value measured by TRMC measurements is the lower limit of the actual mobility of the Ag_3PO_4 particles due to experimental factors, such as inter-particle scattering, surface electron scattering, and/or the quantum yield (ϕ) being lower than unity^{17,27}.

Figures 4(a) and (b) show the TRMC signals ($\phi\sum\mu_i$ versus time) for the tetrahedral and cubic Ag_3PO_4 particles, respectively, under an incident laser pulse with an excitation wavelength of 410 nm with varying intensities I_0 (photon flux measured as photons pulse⁻¹ cm⁻²). The peak values of the TRMC signal ($(\phi\sum\mu_i)_{\text{peak}}$) are plotted versus the photon flux for both cubic and tetrahedral particles in Figure 4(c). The highest $(\phi\sum\mu_i)_{\text{peak}}$ values are obtained at a photon intensity of 8.77×10^{11} photons pulse⁻¹ cm⁻² and represent the highest total mobility (μ_{total}) achieved for the tetrahedral and cubic particles from the TRMC measurement. The tetrahedral particles have a μ_{total} value of $0.56 \text{ cm}^2 \text{ V}^{-1} \text{ s}^{-1}$ and the cubic particles have a μ_{total} value of $0.05 \text{ cm}^2 \text{ V}^{-1} \text{ s}^{-1}$. Hence, the total carrier mobility for the cubic particles is an order of magnitude lower than for the tetrahedral particles (Table 2). The

μ_{total} value of the tetrahedral particles is similar to the mobility obtained for CuFeO_2 ²⁸ and an order of magnitude higher than that obtained for other photoelectrode materials, such as BiVO_4 , $\alpha\text{-SnWO}_4$ and WO_3 ^{18,29,30}. It is two orders of magnitude higher than that of $\alpha\text{-Fe}_2\text{O}_3$ ^{18,29,30}.

The individual electron and hole mobilities for the tetrahedral and cubic particles can be deconvoluted from the total mobility (μ_{total}) using the different effective hole and electron masses for the {111} and {100} surfaces of Ag_3PO_4 as proposed by Umezawa et al.¹⁴ (see equations S3-S4 in supporting information). For the tetrahedral particles with {111} surface, an effective electron mass (m_e^*) of $0.42 m_e$ and an effective hole mass (m_h^*) of $1.53 m_e$ was used¹⁴. For the cubic particles with the {100} surface, a m_e^* of $0.41 m_e$ and a m_h^* of $1.92 m_e$ was used¹⁴. The calculated individual electron and hole mobilities are listed in Table 2. Due to the lower effective mass of the electrons in both tetrahedral and cubic particles, the electron mobility is higher than the hole mobility. Also, both electron and hole mobilities of the tetrahedral particles are more than one order of magnitude higher than the respective mobilities of the cubic particles, as expected from the difference in their μ_{total} values.

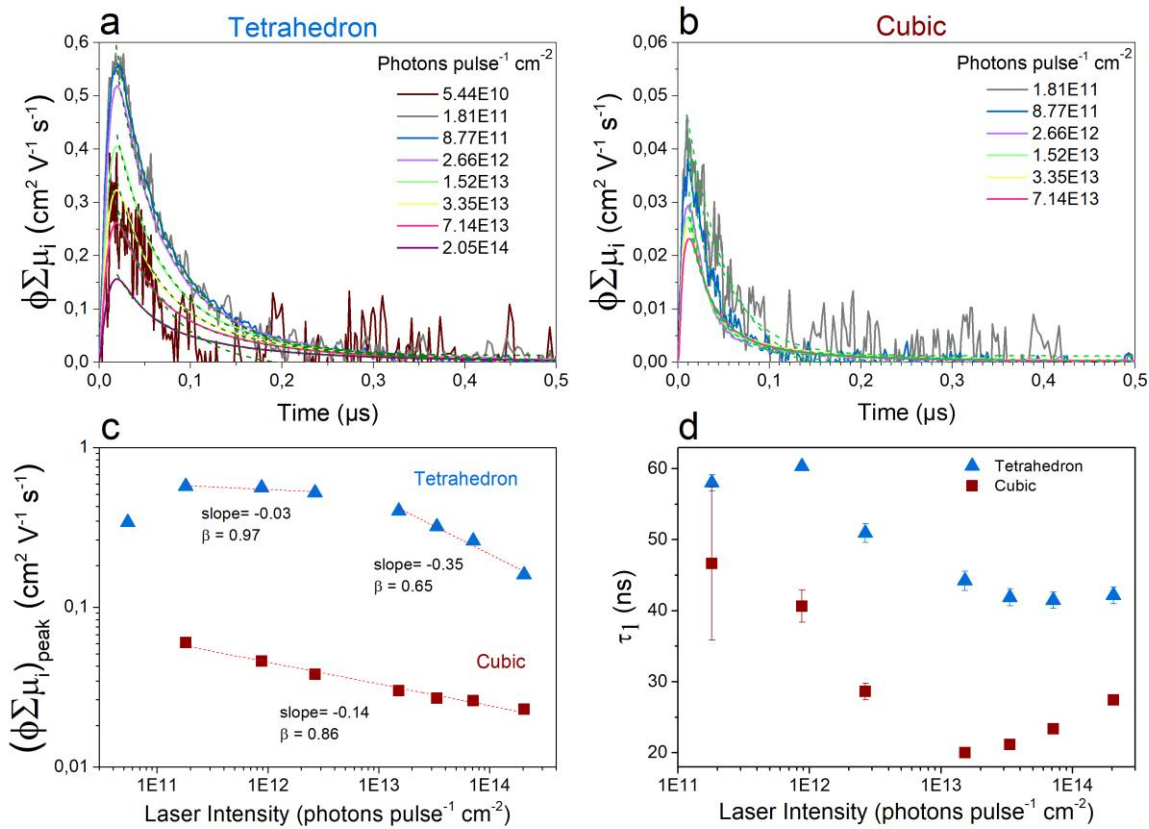


Figure 4 Time resolved microwave conductivity (TRMC) signals recorded for (a) tetrahedral particles and (b) cubic particles using a 410 nm laser pulse with varying photon flux. The dotted lines represent the exponential fit of the TRMC signal; (c) Log-log plot of the maximum observed TRMC signal ($\phi \Sigma \mu_{\text{peak}}$) as a function of incident photon flux. Red lines are linear fits, (d) the first time constant (τ_1) obtained from the bi-exponential fit of the TRMC signals for both particles.

The order of the recombination process occurring in the particles can be obtained by performing a linear fit of the log-log plot of $\phi \Sigma \mu_{\text{peak}}$ versus incident photon flux, I_0 (Figure 4(c)). The slope

obtained from the linear fit is used to obtain the order of the recombination process from the relation $\varphi\Sigma\mu \propto I_o^{\beta-1}$, where β is the reciprocal of the order of recombination process³¹. A first order recombination process, such as a trap state-mediated recombination process, depends only on the density of the minority charge carriers (holes in the case of n-type materials, such as Ag₃PO₄). On the other hand, a second order recombination process, such as a band-to-band recombination process, depends on both the electron and the hole densities.

Differences are observed in the trend of $(\varphi\Sigma\mu)_{\text{peak}}$ values with photon flux for the two differently faceted particles. In the case of cubic particles, the $(\varphi\Sigma\mu)_{\text{peak}}$ values decrease linearly with increasing intensity with a slope of -0.14. Based on the slope of the log-log plot, a β value of 0.86 was determined leading to a recombination order of 1.2. This indicates that both first order (trap-state mediated) and second order (band-to-band) recombination processes are occurring in the cubic particles.^{28,31}

For the tetrahedral particles on the other hand, the $(\varphi\Sigma\mu)_{\text{peak}}$ value increases until it reaches a maximum at an intensity of 8.77×10^{11} photons pulse⁻¹ cm⁻² and then decreases. This behaviour has also been reported elsewhere and has been interpreted as a signature for trap-mediated recombination in semiconductors.^{17,18,31} Essentially, at lower light intensities, the concentration of trap states is higher than the number of absorbed photons. This means that the mobility will increase until all the trap states are filled and then decrease due to higher-order recombination processes. The maximum in mobility is followed by a region where $\beta = 0.97$. This is close to a first-order recombination process which suggests mostly trap state-mediated recombination in this intensity regime. Further increase in laser intensity results in a slope of $\beta = 0.56$ which would suggest mostly second order recombination at these higher light intensities.

It should be noted that although such a behaviour is not observed for the cubic particles in the range of laser intensities studied in this work, trap-state recombination might still occur at light intensities lower than 10^{11} photons pulse⁻¹ cm⁻². However, this cannot be studied due to the poor signal-to-noise ratio for the TRMC signal for the cubic particle at such low light intensities. In any case it suggests that a much higher density of trap states is present in the tetrahedral particles as compared to the cubic particles.

The charge carrier lifetimes are obtained by fitting of the TRMC signal decay at varying laser intensities using a bi-exponential fit. This yields in two time constants, namely τ_1 with values from 20 ns to 60 ns (see Figure 4(d)) and τ_2 with values between 120 ns and 180 ns. The shorter time constant τ_1 is related to the free charge carrier lifetime. τ_1 has a maximum value of 60 ns for the tetrahedral particles and 41 ns for the cubic particles at a laser intensity of 8.77×10^{11} photons pulse⁻¹ cm⁻² (see Table 2). The longer time constant τ_2 is usually attributed to trapped charge carriers.²⁸

From the charge carrier lifetime (τ_1) and the mobility (μ_{total}), the free carrier diffusion length can be calculated using the formula, $L_D = \sqrt{D\tau_1}$, where D is the diffusion coefficient of the charge carriers ($D = (k_b T \mu_{\text{total}} / e)$ where k_b is the Boltzmann constant, T is the temperature, and e is the elementary charge). Using μ_{total} from Table 2 and a temperature $T = 298$ K, the diffusion lengths are 291 nm and 72 nm in tetrahedral and cubic particles, respectively (Table 2). Hence, the diffusion length in tetrahedral particles is 4 times longer than in cubic particles. The diffusion length obtained for the tetrahedral particles is similar to the highest values reported for CuFeO₂²⁸ and about 4 to 5 times higher than for BiVO₄, WO₃ and α -Fe₂O₃^{18,29,30}.

Furthermore, from the electron and hole mobilities, the electron and hole diffusion lengths can also be obtained (see equations S5-S8 and Table S1 in supporting information). The minority carrier

(hole) diffusion length is of particular importance for this material in order to insure high OER activity. For the {111} surface of the tetrahedral particles, the calculated hole diffusion length is 135 nm, while it is 30 nm for the {100} surface of the cubic particles. Thus, the much higher minority carrier diffusion length because of differences in the effective masses for the two facets are a reason for the superior photocatalytic activity for the {111}-faceted tetrahedral particles.

Table 2 Total charge carrier mobility, and individual hole and electron mobilities (calculated from Eq. S3-S4 in the supporting information) as well as lifetimes and diffusion lengths for the tetrahedral and cubic Ag₃PO₄ particles, respectively. Reported values for TRMC measurements with a 410 nm laser at an intensity of 8.77 x 10¹¹ photons pulse⁻¹ cm⁻².

Particle type	Total mobility μ_{total} (cm ² V ⁻¹ s ⁻¹)	Hole mobility μ_{h} (cm ² V ⁻¹ s ⁻¹)	Electron mobility μ_{e} (cm ² V ⁻¹ s ⁻¹)	Charge carrier lifetime τ_1 (ns)	Diffusion length L_D (nm)
Tetrahedral	0.56	0.12	0.44	60	291
Cubic	0.05	0.009	0.041	41	72

DISCUSSION

Various factors result in the better photocatalytic OER performance of the {111}-faceted tetrahedral Ag₃PO₄ particles compared to the {100}-faceted cubic particles as explored by XPS and TRMC measurements. The results presented in the previous section and their interpretation allow understanding these factors and are discussed in the following.

A major factor leading to the better performance of the tetrahedral particles is the superior charge carrier transport properties as compared to the cubic particles. The charge carrier mobility (μ_{total}) is 10 times higher and the carrier diffusion length (L_D) is 4 times higher for the tetrahedral particles compared to the cubic particles (see Table 2). This allows for more efficient charge carrier separation and can therefore lead to better photocatalytic performance. Furthermore, the difference in the calculated hole effective masses for the {111}- and {100}-facets of Ag₃PO₄ leads to 5 times higher minority carrier (hole) diffusion length for the tetrahedral particles. This higher minority carrier diffusion length also contributes to better photocatalytic activity of the {111}-faceted tetrahedral particles.

Another important factor that impacts the performance, is the difference in the surface composition of the different particles (Figure 3). While the {111} particles have a highly P-rich surface, the {100} particles showed a slightly Ag-rich surface. The highly P-rich surface of the tetrahedral particles has been shown theoretically to lead to the presence of 'dangling' P-O bonds^{7,15}. DFT calculations showed that these dangling bonds can enhance the photocatalytic activity of the tetrahedral surface⁶, since they demonstrate low free energy change for the dehydrogenation of water molecules, which is the first step in the oxygen evolution reaction⁷. These P-O bonds can therefore act as shallow trap states which can capture holes, and due to the high reactivity of these dangling bonds towards water dehydrogenation, the captured holes can take part in the OER reaction process. The high concentration of P at the {111} surface, as found

from the XPS analysis, suggests the presence of a large amount of these P-O bonds which can lead to a high density of shallow trap states. This also explains the appearance of a maximum in the $(\Sigma\phi\mu_i)_{\text{peak}}$ versus laser intensity plot in the TRMC measurements (Figure 4(c)); such a maximum is a signature of trap-state recombination due to high trap-state density^{17,18,31}.

On the other hand, the presence of Ag on the {100} surface of cubic particles seems to result in the presence of mid-bandgap trap states or 'deep traps', as reported in DFT calculations by Ma et al.⁷ Deep traps are theoretically found to be much less reactive and are proposed to mainly act as recombination centres for the charge carriers without contribution of the holes trapped in these deep traps to the OER process⁷. Therefore, the presence of deep trap states is believed to be the reason for the lower photocatalytic activity of the cubic particles. However, the amount of excess Ag concentration at the {100} surface of cubic particles is observed to be much lower than the excess P concentration on the {111} surface of the tetrahedral particles. This implies that the density of deep trap states is lower for the cubic particles than the density of shallow traps for the tetrahedral particles. The lower density of these deep trap states also explains the lack of a maxima in the $(\Sigma\phi\mu_i)_{\text{peak}}$ versus laser intensity plot from the TRMC measurements for the cubic particles (Figure 4(c)). It is possible that the $(\Sigma\phi\mu_i)_{\text{peak}}$ plot would also have a maximum when going to lower laser intensities. However, this is not possible due to the poor signal-to-noise ratio at such low laser intensity values.

Based on the TRMC and XPS analyses, schematics of the bands diagrams for the cubic and the tetrahedral particles are drawn in Figure 5. The positions and densities of the trap-states are a representation based on the DFT calculations and are approximated based on the surface composition and the trap-state recombination effects observed from the TRMC measurements. Arrows represent charge transfers. For the cubic particles, the presence of Ag at the surface points towards the existence of deep trap states and are shown as a curve in the mid-bandgap region with the smaller area under the curve representing lower density of these states. These trap states can lead to higher recombination rates (shown by the thick red lines in the schematic) and, hence, to lower charge transfer rates from the VB edge (shown by the thin purple line). This is believed to result in the lower photocatalytic performance of cubic particles. On the other hand, the shallow traps formed as a result of P-O dangling bonds at the surface of tetrahedral particles are shown closer to the VB edge. Furthermore, the maximum in the $(\Sigma\phi\mu_i)_{\text{peak}}$ plot suggests that there might be a higher density of these shallow trap states which is represented by a larger area under the curve. The high density of these shallow states should lead to a larger number of holes captured and the high reactivity of these states can result in higher charge transfer rates from the trap states (shown by the thick green arrow). The faster charge carrier dynamics combined with the high density of reactive trap states is proposed to be the reason for the higher photocatalytic activity of the tetrahedral particles. Charge transfer also occurs from the VB edge, but it is less significant (shown by thin purple line), since most charge carriers will be trapped at the shallow, reactive trap states.

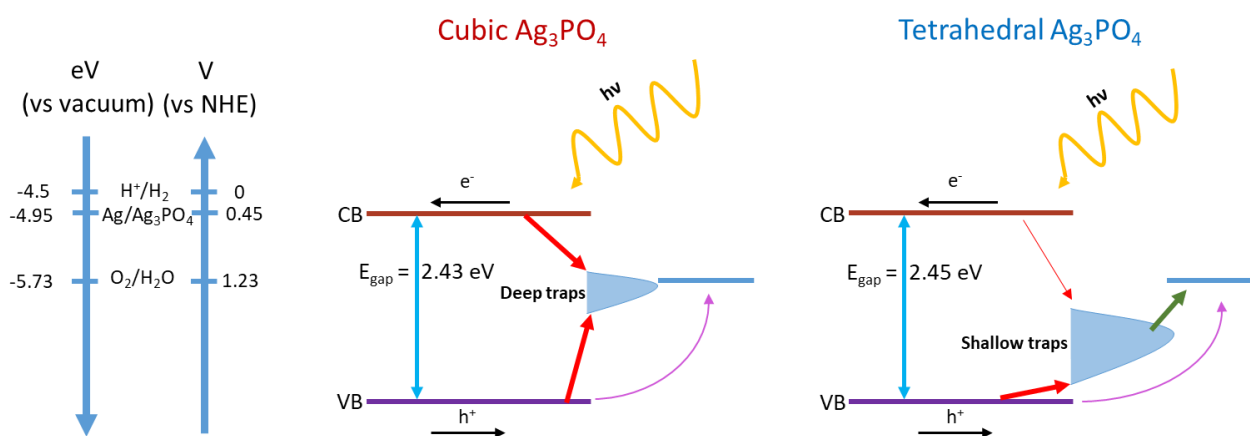


Figure 5 Schematic of the band diagrams for cubic and tetrahedral Ag_3PO_4 particles. Red arrows represent charge capture and recombination; green arrow represents hole transfer from trap states; and the purple arrows represent hole transfer from the valence band (VB) edge. The thickness of the arrow represents the rate of recombination or hole transfer occurring, with thicker lines representing higher rates. The area under the curve for the trap states is a qualitative representation of the density of trap states. The energy level of trap states is considered as the position of centre of the peak relative to the valence band and is a qualitative representation based on DFT calculations on Ag_3PO_4 surfaces⁷.

CONCLUSION

We find that {111}-faceted tetrahedral Ag_3PO_4 particles show higher photocatalytic performance than the {100}-faceted cubic particles. This is explained by investigating the surface composition in combination with the charge carrier dynamics using XPS and time-resolved microwave conductivity (TRMC) measurements. From TRMC, we find that the tetrahedral particles have an order of magnitude higher mobility and a higher minority (hole) carrier diffusion length as compared to the cubic particles. This leads to better charge carrier separation for the tetrahedral particles leading to better photocatalytic performance. Furthermore, TRMC results suggest that tetrahedral particles have a higher density of trap states than cubic particles.

From XPS, it is found that the {111} surface has a high density of P atoms. DFT calculations on the {111} Ag_3PO_4 surface have shown that these P atoms possibly exist in the form of unsaturated P-O 'dangling' bonds, which were theoretically seen to have high reactivity towards water dehydrogenation. Therefore, these dangling P-O bonds possibly act as highly reactive shallow trap states which can lead to an increase of the photocatalytic activity of the tetrahedral particles. On the other hand, the {100} surface in cubic particles has a small density of Ag atoms, which were theoretically shown to form deep trap states and are believed to act as recombination centres. This can lead to reduced photocatalytic activity.

Thus, we find that fabricating particles with different exposed facets leads to differences in the photocatalytic performance of Ag_3PO_4 which is related to a combination of differences in charge carrier transport properties and differences in the nature of the trap states. The {111}-exposed facets of the tetrahedral particles demonstrate better charge carrier transport properties and have a P-rich surface which facilitates water dehydrogenation. This study clarifies experimentally why different facets of Ag_3PO_4 have such different performance and impressively illustrates the importance of facet engineering for the development of highly performing catalytic systems.

SUPPLEMENTARY MATERIAL

The supplementary materials contains X-ray diffraction and high resolution X-ray photo-electron spectroscopy data as well as calculations related to time-resolved microwave conductivity measurements, such as calculations of the electron and hole diffusion lengths.

ACKNOWLEDGEMENT

Sinha, Bieberle-Hütter, and van de Sanden acknowledge the financial support from NWO (FOM program number 147 “CO₂ neutral fuels”). Nanolab at TU Eindhoven is acknowledged for access to SEM and XPS. We would like to thank Michail Tsampas, DIFFER, for his valuable comments on the manuscript and Andrea Baldi, DIFFER, for fruitful discussions.

Data Availability Statement

The data that support the findings of this study are available from the corresponding author upon reasonable request. Additional data supporting the results in the manuscript and the discussions are presented in the supplement information.

REFERENCES

- ¹ M.G. Walter, E.L. Warren, J.R. McKone, S.W. Boettcher, Q. Mi, E.A. Santori, and N.S. Lewis, *Chem. Rev.* **110**, 6446 (2010).
- ² R. van de Krol and M. Grätzel, *Photoelectrochemical Hydrogen Production* (2011).
- ³ H.M. Chen, C.K. Chen, R.-S. Liu, L. Zhang, J. Zhang, and D.P. Wilkinson, *Chem. Soc. Rev.* **41**, 5654 (2012).
- ⁴ K. Sivula, F. Le Formal, and M. Grätzel, *ChemSusChem* **4**, 432 (2011).
- ⁵ Z. Yi, J. Ye, N. Kikugawa, T. Kako, S. Ouyang, H. Stuart-Williams, H. Yang, J. Cao, W. Luo, Z. Li, Y. Liu, and R.L. Withers, *Nat. Mater.* **9**, 559 (2010).
- ⁶ D.J. Martin, G. Liu, S.J.A. Moniz, Y. Bi, A.M. Beale, J. Ye, and J. Tang, *Chem. Soc. Rev.* **44**, 3 (2015).
- ⁷ Z. Ma, S. Lin, R. Sa, Q. Li, and K. Wu, *RSC Adv.* **7**, 23994 (2017).
- ⁸ A.J. Bard, *J. Photochem.* **10**, 59 (1979).
- ⁹ D.J. Martin, N. Umezawa, X. Chen, J. Ye, and J. Tang, *Energy Environ. Sci.* **6**, 3380 (2013).
- ¹⁰ Y. Bi, S. Ouyang, N. Umezawa, J. Cao, and J. Ye, *J. Am. Chem. Soc.* **133**, 6490 (2011).
- ¹¹ X. Cao, X. Zhang, R. Sinha, S. Tao, and A. Bieberle-Hütter, *Phys. Chem. Chem. Phys.* **21**, 9531 (2019).
- ¹² M.H. Huang, M. Madasu, *Nano Today* **28**, 100768 (2019).
- ¹³ C.-S. Tan, Y. Zhao, R.-H. Guo, W.-T. Chuang, L.-J. Chen, M.H. Huang, *Nano Lett.* **20**, 1952 (2020).¹⁴ N. Umezawa, O. Shuxin, and J. Ye, *Phys. Rev. B - Condens. Matter Mater. Phys.* **83**, 1 (2011).
- ¹⁵ S. Kim, Y. Wang, M. Zhu, M. Fujitsuka, and T. Majima, *Chem. - A Eur. J.* **24**, 14928 (2018).
- ¹⁶ R. Miyasato, M. Fujiwara, H. Sato, T. Yano, and H. Hashimoto, *Chem. Phys. Lett. X* (2019).

- ¹⁷ J.E. Kroeze, T.J. Savenije, and J.M. Warman, *J. Am. Chem. Soc.* **126**, 7608 (2004).
- ¹⁸ J.-W. Jang, D. Friedrich, S. Müller, M. Lamers, H. Hempel, S. Lardhi, Z. Cao, M. Harb, L. Cavallo, R. Heller, R. Eichberger, R. van de Krol, and F.F. Abdi, *Adv. Energy Mater.* **7**, 1701536 (2017).
- ¹⁹ Y. Bi, H. Hu, S. Ouyang, G. Lu, J. Cao, and J. Ye, *Chem. Commun.* **48**, 3748 (2012).
- ²⁰ M.S. Hsieh, H.J. Su, P.L. Hsieh, Y.W. Chiang, and M.H. Huang, *ACS Appl. Mater. Interfaces* **9**, 39086 (2017).
- ²¹ Z.L. Wang, *J. Phys. Chem. B* **104**, 1153 (2000).
- ²² F. Parrino, V. Loddo, V. Augugliaro, G. Camera-Roda, G. Palmisano, L. Palmisano, and S. Yurdakal, *Catal. Rev.* **61**, 163 (2019).
- ²³ G. Camera-Roda, V. Loddo, L. Palmisano, and F. Parrino, *Catal. Today* **281**, 221 (2017).
- ²⁴ Kubelka and Munk, *Zeit. Für Tekn. Phys.* **12**, (1931).
- ²⁵ A. Indra, P.W. Menezes, M. Schwarze, and M. Driess, *New J. Chem.* **38**, 1942 (2014).
- ²⁶ B. Zheng, X. Wang, C. Liu, K. Tan, Z. Xie, and L. Zheng, *J. Mater. Chem. A* **1**, 12635 (2013).
- ²⁷ T.J. Savenije, A.J. Ferguson, N. Kopidakis, and G. Rumbles, *J. Phys. Chem. C* **117**, 24085 (2013).
- ²⁸ M.S. Prévot, X.A. Jeanbourquin, W.S. Bourée, F. Abdi, D. Friedrich, R. van de Krol, N. Guijarro, F. Le Formal, and K. Sivula, *Chem. Mater.* **29**, 4952 (2017).
- ²⁹ M. Kölbach, I.J. Pereira, K. Harbauer, P. Plate, K. Höflich, S.P. Berglund, D. Friedrich, R. van de Krol, and F.F. Abdi, *Chem. Mater.* **30**, 8322 (2018).
- ³⁰ S. Hilliard, G. Baldinozzi, D. Friedrich, S. Kressman, H. Strub, V. Artero, and C. Laberty-Robert, *Sustain. Energy Fuels* **1**, 145 (2017).
- ³¹ F.F. Abdi, T.J. Savenije, M.M. May, B. Dam, and R. van de Krol, *J. Phys. Chem. Lett.* **4**, 2752 (2013).